

Thermal properties of graphene: Fundamentals and applications

Eric Pop, Vikas Varshney, and Ajit K. Roy

Graphene is a two-dimensional (2D) material with over 100-fold anisotropy of heat flow between the in-plane and out-of-plane directions. High in-plane thermal conductivity is due to covalent sp^2 bonding between carbon atoms, whereas out-of-plane heat flow is limited by weak van der Waals coupling. Herein, we review the thermal properties of graphene, including its specific heat and thermal conductivity (from diffusive to ballistic limits) and the influence of substrates, defects, and other atomic modifications. We also highlight practical applications in which the thermal properties of graphene play a role. For instance, graphene transistors and interconnects benefit from the high in-plane thermal conductivity, up to a certain channel length. However, weak thermal coupling with substrates implies that interfaces and contacts remain significant dissipation bottlenecks. Heat flow in graphene or graphene composites could also be tunable through a variety of means, including phonon scattering by substrates, edges, or interfaces. Ultimately, the unusual thermal properties of graphene stem from its 2D nature, forming a rich playground for new discoveries of heat-flow physics and potentially leading to novel thermal management applications.

Introduction

Graphene is a two-dimensional (2D) material, formed of a lattice of hexagonally arranged carbon atoms. The term graphene is typically applied to a single layer of graphite, although common references also exist to bilayer or trilayer graphene. (See the introductory article in this issue.) Most thermal properties of graphene are derived from those of graphite and bear the imprint of the highly anisotropic nature of this crystal.¹ For instance, the in-plane covalent sp^2 bonds between adjacent carbon atoms are among the strongest in nature (slightly stronger than the sp^3 bonds in diamond), with a bonding energy² of approximately 5.9 eV. By contrast, the adjacent graphene planes within a graphite crystal are linked by weak van der Waals interactions² (~ 50 meV) with a spacing³ of $h \approx 3.35$ Å. **Figure 1a** displays the typical ABAB (also known as Bernal) stacking of graphene sheets within a graphite crystal.

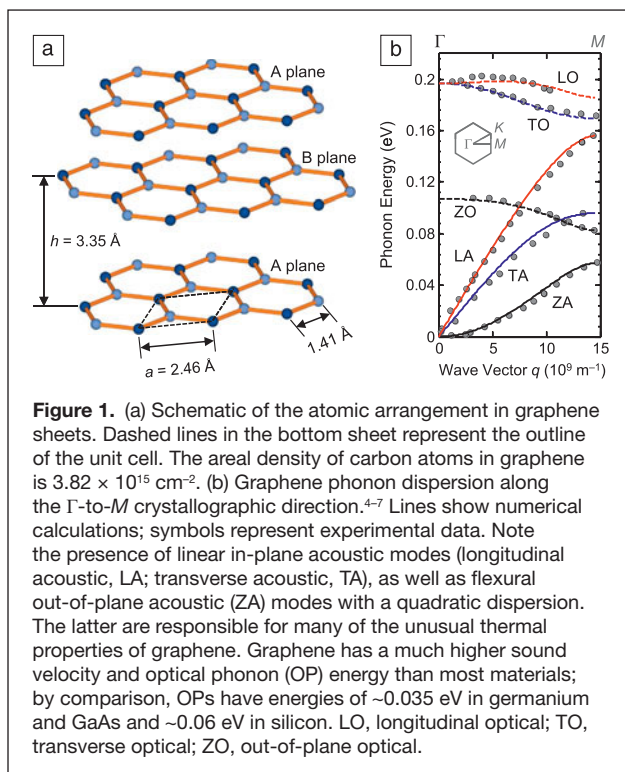
The strong and anisotropic bonding and the low mass of the carbon atoms give graphene and related materials unique thermal properties. In this article, we survey these unusual properties and their relation to the character of the underlying lattice vibrations. We examine both the specific heat and thermal conductivity of graphene and related materials and the conditions for achieving ballistic, scattering-free heat flow. We also

investigate the role of atomistic lattice modifications and defects in tuning the thermal properties of graphene. Finally, we explore the role of heat conduction in potential device applications and the possibility of architectures that allow control over the thermal anisotropy.

Phonon dispersion of graphene

To understand the thermal properties of graphene, one must first inspect the lattice vibrational modes (phonons) of the material. The graphene unit cell, marked by dashed lines in Figure 1a, contains $N = 2$ carbon atoms. This leads to the formation of three acoustic (A) and $3N - 3 = 3$ optical (O) phonon modes, with the dispersions⁴⁻⁷ shown in Figure 1b. The dispersion is the relationship between the phonon energy E or frequency ω ($E = \hbar\omega$, where \hbar is the reduced Planck constant) and the phonon wave vector q . Longitudinal (L) modes correspond to atomic displacements along the wave propagation direction (compressive waves), whereas transverse (T) modes correspond to in-plane displacements perpendicular to the propagation direction (shear waves). In typical three-dimensional (3D) solids, transverse modes can have two equivalent polarizations, but the unique 2D nature of graphene allows out-of-plane atomic displacements, also known as flexural (Z) phonons.

Eric Pop, University of Illinois at Urbana-Champaign; epop@illinois.edu
Vikas Varshney, Air Force Research Laboratory; vikas.varshney@wpafb.af.mil
Ajit K. Roy, Air Force Research Laboratory; ajit.roy@wpafb.af.mil
DOI: 10.1557/mrs.2012.203



At low q near the center of the Brillouin zone, the frequencies of the transverse acoustic (TA) and longitudinal acoustic (LA) modes have linear dispersions^{8,9} of $\omega_{\text{TA}} \approx v_{\text{TA}}q$ and $\omega_{\text{LA}} \approx v_{\text{LA}}q$, respectively. The group velocities $v_{\text{TA}} \approx 13.6 \text{ km/s}$ and $v_{\text{LA}} \approx 21.3 \text{ km/s}$ are four to six times higher than those in silicon or germanium because of the strong in-plane sp^2 bonds of graphene and the small mass of carbon atoms.^{8–11} In contrast, the flexural ZA modes have an approximately quadratic dispersion,^{8,9} $\omega_{\text{ZA}} \approx aq^2$, where $a \approx 6.2 \times 10^{-7} \text{ m}^2/\text{s}$. As we will discuss, the existence and modifications of these ZA modes are responsible for many of the unusual thermal properties of graphene.

Specific heat of graphene and graphite

The specific heat, C , of a material represents the change in energy density U when the temperature changes by 1 K, $C = dU/dT$, where T is the absolute temperature. The specific heat and heat capacity are sometimes used interchangeably, with units of joules per kelvin per unit mass, per unit volume, or per mole. The specific heat determines not only the thermal energy stored within a body but also how quickly the body cools or heats, that is, its thermal time constant $\tau \approx RCV$, where R is the thermal resistance for heat dissipation (the inverse of conductance, $R = 1/G$) and V is the volume of the body. Thermal time constants can be very short for nanoscale objects, on the order of 10 ns for nanoscale transistors,¹² 0.1 ns for a single graphene sheet or carbon nanotube (CNT),¹³ and 1 ps for the relaxation of individual phonon modes.^{14–16}

The specific heat of graphene has not been measured directly; thus, the short discussion here refers to experimental

data available for graphite.^{17–19} The specific heat is stored by the lattice vibrations (phonons) and the free conduction electrons of a material, $C = C_p + C_e$. However, phonons dominate the specific heat of graphene at all practical temperatures^{19,20} ($>1 \text{ K}$), and the phonon specific heat increases with temperature,^{17–20} as shown in **Figure 2**. At very high temperatures²² (approaching the in-plane Debye temperature^{17,24} $\Theta_D \approx 2100 \text{ K}$), the specific heat is nearly constant at $C_p = 3N_A k_B \approx 25 \text{ J mol}^{-1} \text{ K}^{-1} \approx 2.1 \text{ J g}^{-1} \text{ K}^{-1}$, also known as the Dulong–Petit limit. Here, N_A is Avogadro’s number, and k_B is the Boltzmann constant. This is the “classical” behavior of solids at high temperature when all six atomic degrees of motion (three translational and three vibrational) are excited and each carries $\frac{1}{2}k_B T$ energy.

At room temperature, the specific heat of graphite is $C_p \approx 0.7 \text{ J g}^{-1} \text{ K}^{-1}$, approximately one-third of the classical upper limit.^{17,19} Interestingly, this value for graphite at room temperature is $\sim 30\%$ higher than that of diamond because of the higher density of states at low phonon frequencies given by the weak coupling between graphite layers.¹⁷ A similar behavior is expected for an isolated graphene sheet at room temperature, when all of its flexural ZA modes should be thermally excited. However, it is possible that these modes could be partly suppressed or their dispersion altered when graphene is in strong contact with a substrate (thus lowering the specific heat), as suggested by experiments investigating epitaxial graphene on metals^{25,26} and recent theoretical work concerning graphene on insulators.²⁷

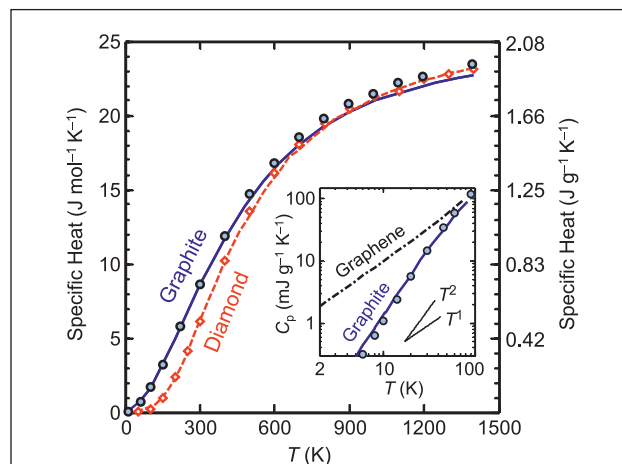


Figure 2. Specific heats of graphene, graphite, and diamond, all dominated by phonons at temperatures above $\sim 1 \text{ K}$. Lines show numerical calculations;^{10,17,21} symbols represent experimental data.^{19,22,23} The inset indicates that the low-temperature specific heat of an isolated graphene sheet is expected to be higher than that of graphite because of the contribution of low-frequency ZA phonons (also see Figure 1b). Above $\sim 100 \text{ K}$, the specific heats of graphene and graphite should be identical. The inset makes use of different units to illustrate a common occurrence in practice (e.g., $\text{J mol}^{-1} \text{ K}^{-1}$, or $\text{J g}^{-1} \text{ K}^{-1}$, or $\text{J cm}^{-3} \text{ K}^{-1}$), but conversion is easily achieved by dividing and/or multiplying by the atomic mass of carbon ($A = 12.01 \text{ g/mol}$) or the density of graphite ($\rho \approx 2.25 \text{ g/cm}^3$).

At low temperatures (Figure 2 inset), the specific heat scales as $C_p \sim T^{d/n}$ for a phonon dispersion of $\omega \sim q^n$ in d dimensions.^{10,21} Thus, the low-temperature specific heat contains valuable information about both the dimensionality of a system and its phonon dispersion.²¹

The behavior of C_p for an isolated graphene sheet should be linear in T at very low temperatures when the quadratic ZA modes dominate, followed by a transition to $\sim T^2$ behavior due to the linear LA and TA phonons^{10,20,21} and eventually by a “flattening” to a constant as the high Debye temperature Θ_D is approached, in the classical limit (Figure 2). Indeed, numerical calculations using the complete phonon dispersion^{10,21} reveal that, for a wide temperature range ($T < 50$ K), C_p is linear in T for isolated graphene, as shown in the Figure 2 inset. By contrast, the specific heat of graphite rises as $\sim T^3$ at very low temperature (< 10 K) due to the weak interlayer coupling.¹⁸ In an intermediate temperature range (10–100 K), the C_p value of graphite transitions to $\sim T^2$ behavior because of the in-plane linear phonons once the soft c -axis modes are fully occupied.²⁰ This behavior is consistent with graphite having both 2D and 3D features and is shown in the Figure 2 inset. Calculations¹⁹ and recent measurements²⁸ have also estimated the specific heat of the electronic gas in graphene at low temperature, finding values on the order of $C_e \approx 2.6 \mu\text{J g}^{-1} \text{K}^{-1}$ at 5 K (three orders of magnitude lower than the phonon specific heat, C_p , at this temperature). The value of C_e in graphene is lower than those in other 2D electron gases, opening up interesting opportunities for graphene as a fast and sensitive bolometric detector.²⁸

Thermal conductivity of graphene: Intrinsic

The thermal conductivity (κ) of a material relates the heat flux per unit area, Q'' (e.g., in W/m^2), to the temperature gradient, $Q'' = -\kappa \nabla T$. The sign in this relationship is negative, indicating that heat flows from high to low temperature. The thermal conductivity can be related to the specific heat by $\kappa \approx \sum C_v \lambda$, where v and λ are the appropriately averaged phonon group velocity and mean free path, respectively.²⁹ This expression is commonly used under diffusive transport conditions, when sample dimensions are much greater than the phonon mean free path ($L \gg \lambda$). (We discuss the ballistic heat-flow regime in a later section.) For the purposes of heat transport, the “thickness” of a graphene monolayer is typically assumed to be the graphite interlayer spacing,³ $h \approx 3.35 \text{ \AA}$.

The in-plane thermal conductivity of graphene at room temperature is among the highest of any known material,

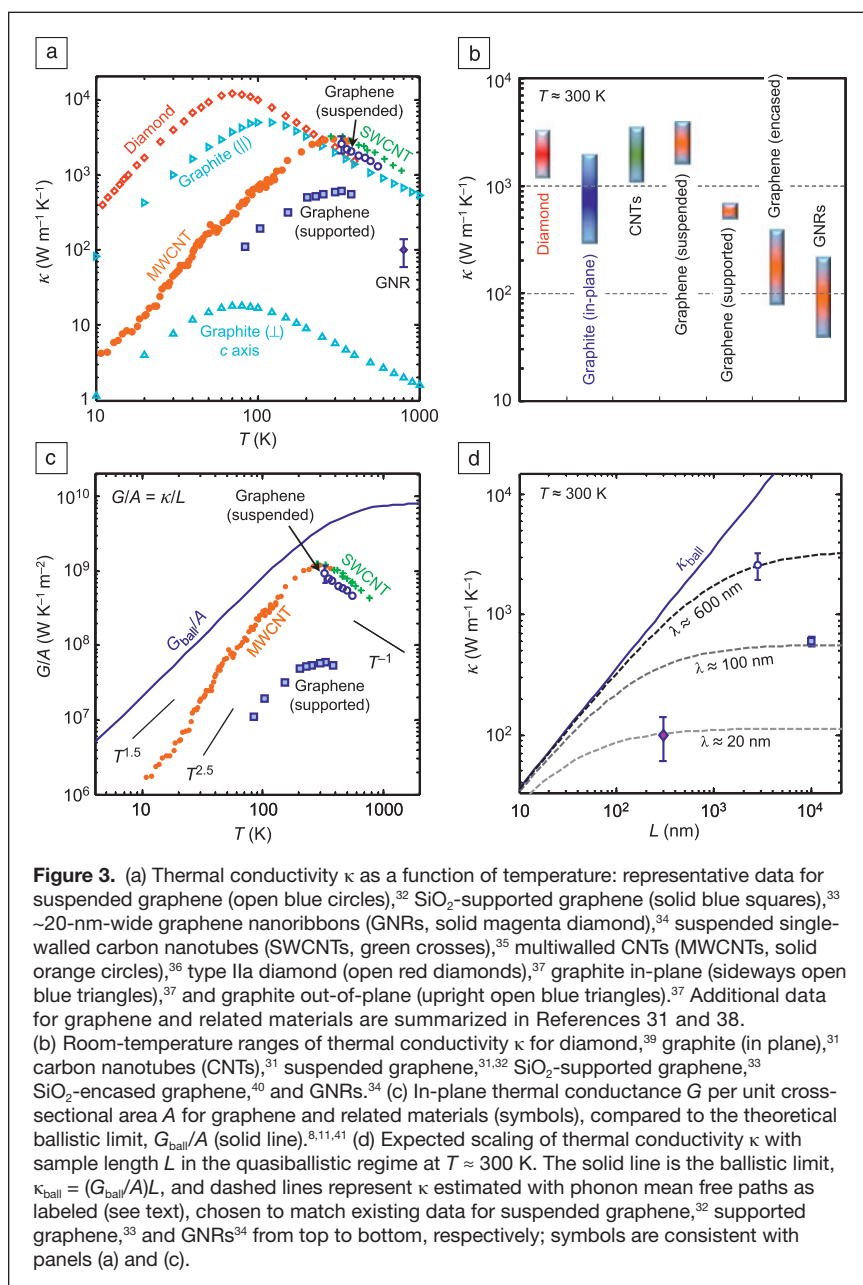


Figure 3. (a) Thermal conductivity κ as a function of temperature: representative data for suspended graphene (open blue circles),³² SiO₂-supported graphene (solid blue squares),³³ ~20-nm-wide graphene nanoribbons (GNRs, solid magenta diamonds),³⁴ suspended single-walled carbon nanotubes (SWCNTs, green crosses),³⁵ multiwalled CNTs (MWCNTs, solid orange circles),³⁶ type IIa diamond (open red diamonds),³⁷ graphite in-plane (sideways open blue triangles),³⁷ and graphite out-of-plane (upright open blue triangles).³⁷ Additional data for graphene and related materials are summarized in References 31 and 38. (b) Room-temperature ranges of thermal conductivity κ for diamond,³⁹ graphite (in plane),³¹ carbon nanotubes (CNTs),³¹ suspended graphene,^{31,32} SiO₂-supported graphene,³³ SiO₂-encased graphene,⁴⁰ and GNRs.³⁴ (c) In-plane thermal conductance G per unit cross-sectional area A for graphene and related materials (symbols), compared to the theoretical ballistic limit, G_{ball}/A (solid line).^{8,11,41} (d) Expected scaling of thermal conductivity κ with sample length L in the quasiballistic regime at $T \approx 300 \text{ K}$. The solid line is the ballistic limit, $\kappa_{\text{ball}} = (G_{\text{ball}}/A)L$, and dashed lines represent κ estimated with phonon mean free paths as labeled (see text), chosen to match existing data for suspended graphene,³² supported graphene,³³ and GNRs³⁴ from top to bottom, respectively; symbols are consistent with panels (a) and (c).

about 2000–4000 $\text{W m}^{-1} \text{K}^{-1}$ for freely suspended samples^{30–32} (Figure 3a–b). The upper end of this range is achieved for isotopically purified samples (0.01% ¹³C instead of 1.1% natural abundance) with large grains,³² whereas the lower end corresponds to isotopically mixed samples or those with smaller grain sizes. Naturally, any additional disorder or even residue from sample fabrication⁴² will introduce more phonon scattering and lower these values further. For comparison, the thermal conductivity of natural diamond is $\sim 2200 \text{ W m}^{-1} \text{K}^{-1}$ at room temperature^{39,43} (that of isotopically purified diamond is 50% higher, or $\sim 3300 \text{ W m}^{-1} \text{K}^{-1}$), and those of other related materials are plotted in Figure 3a–b. In particular, Figure 3b shows presently known ranges of thermal conductivity at room temperature, with the implication

that all lower bounds could be further reduced in more disordered samples.

By contrast, heat flow in the cross-plane direction (along the c axis) of graphene and graphite is strongly limited by weak interplane van der Waals interactions. The thermal conductivity along the c axis of pyrolytic graphite is a mere $\sim 6 \text{ W m}^{-1} \text{ K}^{-1}$ at room temperature,^{1,37} as shown in Figure 3a. Heat flow perpendicular to a graphene sheet is also limited by weak van der Waals interactions with adjacent substrates, such as SiO_2 . The relevant metric for heat flow across such interfaces is the thermal conductance per unit area, $G'' = Q''/\Delta T \approx 50 \text{ MW m}^{-2} \text{ K}^{-1}$ at room temperature.^{44–46} This is approximately equivalent to the thermal resistance of a $\sim 25\text{-nm}$ layer of SiO_2 ¹² and could become a limiting dissipation bottleneck in highly scaled graphene devices and interconnects,³⁴ as discussed in a later section. Interestingly, the thermal resistance, $1/G''$, does not change significantly across few-layer graphene samples⁴⁵ (i.e., from one to 10 layers), indicating that the thermal resistance between graphene and its environment dominates that between individual graphene sheets. Indeed, the interlayer thermal conductance of bulk graphite is $\sim 18 \text{ GW m}^{-2} \text{ K}^{-1}$ if the typical spacing (Figure 1a) and c -axis thermal conductivity are assumed.

Thermal conductivity of graphene: Roles of edges and substrates

Despite its high room-temperature value for freely suspended samples, the in-plane thermal conductivity of graphene decreases significantly when this 2D material is in contact with a substrate or confined in graphene nanoribbons (GNRs). This behavior is not unexpected, given that phonon propagation in an atomically thin graphene sheet is likely to be very sensitive to surface or edge perturbations. At room temperature, the thermal conductivity of graphene supported by SiO_2 ³³ was measured as $\sim 600 \text{ W m}^{-1} \text{ K}^{-1}$, that of SiO_2 -encased graphene⁴⁰ was measured as $\sim 160 \text{ W m}^{-1} \text{ K}^{-1}$, and that of supported GNRs³⁴ was estimated as $\sim 80 \text{ W m}^{-1} \text{ K}^{-1}$ for $\sim 20\text{-nm}$ -wide samples. The broader ranges of presently known values at room temperature are summarized in Figure 3b. Although differences could exist between these studies in terms of defects introduced during sample fabrication, for example, the results nevertheless suggest a clear decrease in thermal conductivity from that of isolated (freely suspended) graphene, consistent with theoretical predictions.^{47–49}

For SiO_2 -supported graphene, the decrease in thermal conductivity occurs as a result of the coupling and scattering of graphene phonons with substrate vibrational modes,¹⁶ such that the graphene ZA branch appears to be most affected.^{27,33} This decrease is also seen in Figure 3c, expressed as thermal conductance per unit cross-sectional area (G/A), which is a more appropriate measure when samples approach ballistic heat-flow limits. For comparison, this figure also displays the thermal conductance of CNTs^{35,36} and the theoretical upper limit of scattering-free ballistic transport (G_{ball}/A) as calculated from the phonon dispersion.^{8,11,41} (Also see the later section on ballistic transport.) Figure 3d illustrates the expected dependence of the room-temperature thermal conductivity on sample length L in a

quasiballistic transport regime, as L becomes comparable to or smaller than the intrinsic phonon mean free path, $\lambda_0 \approx 600 \text{ nm}$. When graphene is confined in GNRs that are narrower than the intrinsic phonon mean free path (width $W \leq \lambda_0$), phonon scattering with boundaries and edge roughness further reduces the thermal conductivity^{48,49} compared to the cases of suspended and SiO_2 -supported graphene.

It is relevant to put such thermal properties of graphene into context. For comparison, the thermal conductivity of thin Si-on-insulator (SOI) films is also strongly reduced from the bulk silicon value ($\sim 150 \text{ W m}^{-1} \text{ K}^{-1}$ at room temperature) to $\sim 25 \text{ W m}^{-1} \text{ K}^{-1}$ in $\sim 20\text{-nm}$ thin films as a result of surface scattering.⁵⁰ This value is further reduced to $\sim 2 \text{ W m}^{-1} \text{ K}^{-1}$ in $\sim 20\text{-nm}$ -diameter silicon nanowires with rough surfaces.⁵¹ At comparable linewidths, the thermal conductivity of copper interconnects is on the order of $\sim 100 \text{ W m}^{-1} \text{ K}^{-1}$ (a factor of four lower than that of bulk copper) based on the Wiedemann–Franz law that relates the thermal and electrical conductivity of metals.⁵² In contrast, despite substrate or edge effects, graphene maintains a relatively high thermal conductivity in 2D monolayer films that are atomically thin ($h \approx 3.35 \text{ \AA}$), a size regime where no 3D materials can effectively conduct heat.

Thermal modeling of graphene

Given that thermal measurements of graphene are challenging because of its atomic thinness, modeling and simulation have played a key role in developing an understanding of graphene properties.⁵³ Existing methods for modeling thermal transport in graphene and GNRs include atomistic techniques such as molecular dynamics (MD),^{16,27,54–60} nonequilibrium Green's functions (NEGF),^{61–64} and Boltzmann transport equation simulations.^{9,33,47,49} The following discussion focuses on MD simulations, which have provided atomistic insights into graphene heat flow and have also predicted novel routes for tailoring the thermal properties of nanostructured graphene materials.

Insights from molecular dynamics

MD is a deterministic approach for investigating properties of molecular systems that employs empirical interactions between atoms as a “force field” and follows classical Newtonian dynamics.⁶⁵ Figure 4a schematically illustrates one of the two nonequilibrium molecular dynamics (NEMD) methodologies that are routinely used to investigate thermal transport in graphene or GNRs. In this methodology, atoms at both ends are kept fixed while near-end portions of a few nanometers are treated as hot and cold regions. By imposing either constant-heat-flux or constant-temperature boundary conditions in the hot and cold regions, a steady-state temperature gradient is introduced within the graphene sheet, which is then used to estimate the material thermal conductivity.

MD simulations have revealed how heat flow can be tuned or altered with respect to that of pristine graphene by introducing atomistic alterations of the honeycomb lattice. Such alterations are achieved through vacancies or Stone–Wales defects,^{48,59,66} grain boundaries,^{67,68} strain,^{69,70} chemical functionalization,⁷¹

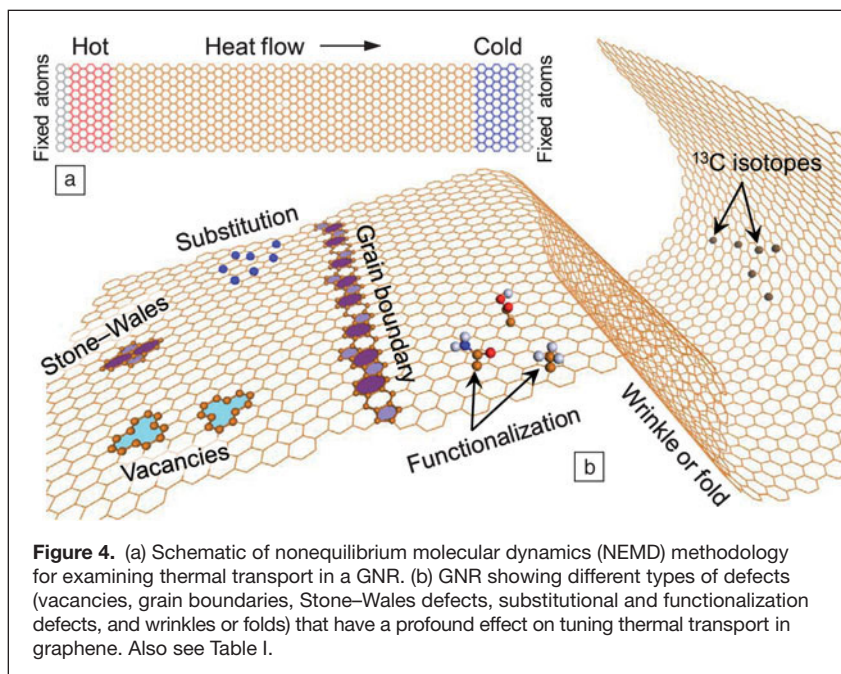


Figure 4. (a) Schematic of nonequilibrium molecular dynamics (NEMD) methodology for examining thermal transport in a GNR. (b) GNR showing different types of defects (vacancies, grain boundaries, Stone–Wales defects, substitutional and functionalization defects, and wrinkles or folds) that have a profound effect on tuning thermal transport in graphene. Also see Table I.

isotopic impurities (¹³C)^{56,57} or substitutional defects,⁵⁸ and edge roughness^{54,55,57} or folding⁶⁴ in GNRs, as shown in Figure 4b. Alterations or defects can reduce the thermal conductivity of graphene by an order of magnitude or more below its intrinsic value, as summarized in **Table I**. Such a reduction in thermal conduction could be interesting for thermoelectric applications, if the high electronic conduction of graphene can be preserved.⁷²

Another interesting feature predicted by thermal MD simulations of graphene is that of thermal rectification. By analogy with electrical rectification in a *p–n* diode, a thermal rectifier would allow greater heat flux in one direction than another, that is, $Q_{BA} > Q_{AB}$ for the same temperature difference $\Delta T_{BA} = \Delta T_{AB}$ between its two terminals A and B.¹² Any type of spatial variability that introduces asymmetry in the phonon density of states of the hot and cold regions has been suggested as a key criterion necessary for thermal rectification. For graphene, such a feature has been identified by MD simulations by introducing either shape asymmetry within the nanostructure (such as a thickness-modulated GNR,⁶⁰ tapered-width GNR,^{54,73} or Y-shaped GNR⁷⁴) or mass asymmetry through substitution with ¹³C isotopes.⁷⁵ In addition, a recent study has also suggested that asymmetry in thermal reservoirs is as essential as system asymmetry in achieving thermal rectification in any system.⁷⁶ No matter how it is achieved, the modulation of directional heat flux could provide novel functionality in future nanoelectronic devices such as thermal rectifiers, thermal transistors, and thermal logic gates.

Nevertheless, the results of MD simulations should be interpreted in the proper context.³⁸ The main strength of the MD approach is that it can be used to analyze the effects of atomistic changes on the thermal properties of a nanomaterial (Figure 4 and Table I). However, MD is a semiclassical technique that overestimates the specific heat below the Debye temperature,

Θ_D . Graphene has a very high Debye temperature, $\Theta_D \approx 2100$ K, such that the specific heat at room temperature is only about one-third that of the classical Dulong–Petit limit (Figure 2). MD results are also sensitive to the choice of interatomic potential.^{59,77} Thus, absolute values of thermal conductivity for graphene and GNRs calculated by MD span a wide range (75–10,000 W m^{−1} K^{−1}; see Table I) because of differences in interatomic potentials,^{59,77} boundary conditions, and simulated system dimensions (often 10 nm or smaller). The effect of system dimensions is more challenging in graphene than in other materials because of the very large intrinsic phonon mean free path, $\lambda_0 \approx 600$ nm (see the next section). Thus, MD simulations should generally be interpreted based on the relative changes rather than the absolute values of the thermal properties they predict. Such changes are listed in the last column of Table I.

Ballistic limit of graphene thermal conductivity

Whereas the classical regime of large sample size ($L \gg \lambda_0$) suggests a constant thermal conductivity, κ , and a thermal conductance that scales inversely with length, $G = \kappa A/L$, quantum treatment of small graphene devices ($L \ll \lambda_0$) reveals that the thermal conductance approaches a constant (G_{ball}), independent of length,^{8,11,41} in ballistic, scattering-free transport. Thus, the relationship between conductivity and conductance imposes that the effective thermal conductivity of a ballistic sample must be proportional to its length as $\kappa_{\text{ball}} = (G_{\text{ball}}/A)L$, where A is the cross-sectional area, $A = Wh$. This is an important distinction also made between the *electrical* conductance, which reaches a constant value (e.g., ~ 155 μS in single-walled CNTs with four quantum channels^{78,79}), and the electrical conductivity and mobility, which appear to depend on the device length in the ballistic regime.^{80,81}

The ballistic thermal conductance of graphene can be numerically calculated^{8,11,41} from the phonon dispersion (Figure 1b) and is shown by the solid line in Figure 3c. This upper ballistic limit can also be approximated analytically⁸ as $G_{\text{ball}}/A \approx 6 \times 10^5 T^{1.5}$ W m^{−2} K^{−5/2} for $T < 100$ K. The $\sim T^{1.5}$ dependence arises from the dominance of flexural ZA modes at low temperatures, with a specific heat $C \sim T$ and a phonon dispersion with $\omega \sim q^2$. A comparison with the currently available experimental data in terms of conductance per unit area (symbols in Figure 3c) reveals that various measurements have reached only a fraction of this ballistic limit. For instance, 10- μm -long graphene supported on SiO₂³³ reached $\sim 2\%$, and 2.8- μm long suspended graphene samples³² reached $\sim 25\%$ of the theoretical ballistic thermal conductance limit at room temperature.

The transition of thermal conductivity from the ballistic ($L \ll \lambda_0$) to the diffusive ($L \gg \lambda_0$) heat-flow regime can be approximated through a Landauer-like approach^{29,82} as $\kappa(L) \approx G_{\text{ball}}/A[1/L + 2/(\pi\lambda)]^{-1}$, where the factor of $\pi/2$ accounts for

Table I. Summary of simulation results for tuning or reduction in thermal conductivity of graphene through various atomistic modifications (also see Figure 4)

Reference	κ of Unmodified Graphene or GNRs ($\text{W m}^{-1} \text{K}^{-1}$)	Atomistic Modification	Degree of Modification	Tuning or Reduction of κ
48	2300 (GNR)	MV, DV	0.1%	~81%, ~69%
		Edge roughness	~7 Å	~80%
		SW dislocations	0.1%	~69%
		Mixed SW/DV (50/50)	0.23%	~81%
54	~670–2000 (GNR)	MV	N/A	~50%
		Edge roughness	N/A	~50%
55	~2500–8000 (GNR)	Edge roughness	N/A	~60% in GNRs
56	~630–1000	Isotopic substitution (^{13}C)	25–75%	~70% at 50% ^{13}C
57	~670–2000 (GNR)	H passivation	N/A	~50%
		Isotopic substitution (^{13}C)	0–100%	~35% at 55% ^{13}C
58	3000 (graphene)	N substitution	3%	~70%
		Curvature	0–350°	~25% at 350
59	2900 (graphene)	Vacancies	8.25%	~1000× decrease
64	112 (supported GNR)	Folding	3–6 folds	~30–70%
66	N/A	Vacancies	4%	~95%
		SW defects	2.3%	~85%
67	2650 (graphene)	GB	22% tilt	~20% at 5.5°
68	~1500 (graphene)	GB	28% tilt	~30%
69	~5500 (graphene)	Strain	±6%	~45%
70	77.3 (zigzag GNR)	Strain	+20%	~60%
	74.7 (armchair GNR)	Strain	~10%	~10%
71	~267–300 (GNR)	Functionalization	10%	~85%

N/A, not available.

DV, diatomic vacancies; GB, grain boundary; MV, monatomic vacancies; SW, Stone–Wales.

angle averaging⁸³ in two dimensions to obtain the backscattering length responsible for the thermal resistance. Fitting this simple expression to the experimental data in Figure 3d reveals phonon mean free paths at room temperature of $\lambda_0 \approx 600$ nm in suspended graphene (also referred to here as the intrinsic mean free path), $\lambda \approx 100$ nm in graphene supported on SiO_2 , and $\lambda \approx 20$ nm in GNRs (of width ~20 nm) supported on SiO_2 . These are some of the key length scales needed for understanding graphene thermal properties in nanometer-size devices. The ballistic upper limit of thermal conductivity in a graphene sample of length $L \approx 100$ nm can now be estimated as $\kappa_{\text{ball}} \approx 350 \text{ W m}^{-1} \text{K}^{-1}$ at room temperature. We note that suspended graphene should attain >80% of the ballistic heat-flow limit in samples shorter than $L < 235$ nm, whereas graphene supported on SiO_2 reaches this level at $L < 40$ nm, well within the means of modern nanofabrication.

Thermal properties for applications Devices and interconnects

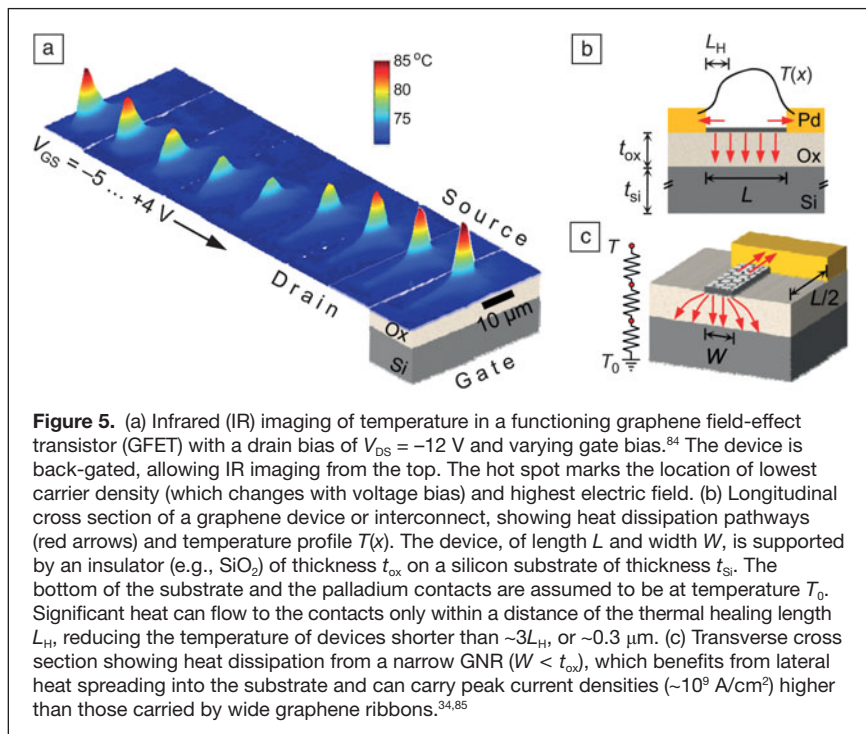
In the context of nanoscale devices and interconnects, graphene is often thought to hold advantages over other materials because of its higher thermal conductivity. Thus, high thermal conductivity could suggest very good heat sinking and low temperature rise during device operation. However, under high-field and high-temperature (i.e., typical circuit) operating conditions, significant dissipation and temperature rise can nevertheless occur in graphene devices,^{34,84} as shown in **Figure 5**.

Self-heating of graphene devices and interconnects at high field begins through the emission of optical phonons (OPs),^{86–88} similarly to the case of CNTs. OPs are strongly emitted at applied voltages comparable to or greater than their energy (~0.16 eV; see Figure 1b), although smaller biases can also be sufficient because of the long Fermi tail of the electron (or hole) distribution. OPs decay on time scales of ~1 ps into lower-energy acoustic phonons (APs).^{14,89} However, given their comparatively large specific heat, the AP temperature lags behind that of the electrons and OPs by ~1–10 ns after a voltage pulse is applied. (This delay also depends on the thermal resistance between the device and the surrounding environment.¹²)

The pathway of heat dissipation to the environment heat sink becomes key in determining the temperature rise once steady state is reached and thus, ultimately, the reliability of graphene devices. In other words, despite (or perhaps because of) the excellent intrinsic thermal properties of graphene, dissipation from graphene devices is often limited by their interfaces, contacts, and surrounding materials, which are often thermal insulators such

as SiO_2 . To illustrate this point, Figure 5a shows temperature profiles recorded by infrared thermal imaging⁸⁴ along a graphene device on SiO_2 under a constant drain–source bias ($V_{\text{DS}} = -12$ V) as the gate voltage (V_{GS}) is varied from –5 V to 4 V. The complex temperature profile occurs because the carrier density and, thus, the electric field are not constant along the device at high bias. Consequently, the temperature hot spot marks the location of maximum electric field and minimum carrier concentration.⁸⁴

A schematic of dissipation in a graphene device is shown in Figure 5b, where heat flow can occur either into the substrate or to the metal contacts.^{34,90} The length scale for lateral heat flow to the contacts is the thermal healing length $L_{\text{H}} \approx (\kappa W h / g)^{1/2}$, where W is the device width, g is the thermal conductance to the substrate per unit length,³⁴ and other symbols are as previously defined. The total thermal conductance g includes



done to adjust the overall device temperature, for example, using asymmetric contacts, from the point of view of either geometry (one larger contact to sink heat) or materials (two contacts with different Seebeck coefficients).

3D architectures

As summarized earlier, because of its 2D nature, graphene has very high anisotropy of its thermal properties between the in-plane and out-of-plane directions. Whereas the in-plane thermal conductivity is excellent ($>1000 \text{ W m}^{-1} \text{ K}^{-1}$), the out-of-plane thermal coupling is limited by weak van der Waals interactions and could become a thermal dissipation bottleneck. To overcome this effect in practice, 3D architectures could incorporate CNT-pillared graphene network (PGN) structures,⁹¹ interconnected CNT truss-like structures,⁹² and networked graphene flakes.⁹³ These 3D architectures (Figure 6) are envisioned as a new generation of nanomaterials with tunable thermomechanical functionality, leveraging the best aspects of both graphene and CNTs. Such structures could

the contribution from the graphene–substrate interface and that from any underlying layers (e.g., SiO_2 and Si in Figure 5b). For typical supporting oxide thicknesses ($t_{\text{ox}} \approx 90\text{--}300 \text{ nm}$) and interfacial thermal conductances G'' , $L_{\text{H}} \approx 0.1\text{--}0.2 \mu\text{m}$.

Numerical calculations suggest that only devices shorter than $\sim 3L_{\text{H}} \approx 0.3\text{--}0.6 \mu\text{m}$ benefit from substantial cooling through the metal contacts.^{34,85} For long devices ($L \gg 3L_{\text{H}}$), the dissipation occurs almost entirely through the graphene–substrate interface (of thermal resistance $1/G''$) and through the underlying substrate (e.g., SiO_2/Si , BN/Si , SiC). For narrow devices ($W < t_{\text{ox}}$) such as GNRs, a substantial amount of lateral heat spreading into the underlying oxide can also play a role,³⁴ as illustrated in Figure 5c. Finally, for devices that are both long and wide ($L, W \gg L_{\text{H}}, t_{\text{ox}}$), the total thermal resistance can be estimated simply as⁸⁷ $R_{\text{th}} \approx 1/(G''A) + t_{\text{ox}}/(\kappa_{\text{ox}}A) + 1/(2\kappa_{\text{Si}}A^{1/2})$, where κ_{ox} and κ_{Si} are the thermal conductivities of SiO_2 and silicon, respectively; $A = LW$ is the device area; and other variables are as defined in Figure 5. The final term approximates the spreading thermal resistance in the silicon substrate, which is assumed to be much thicker than both t_{ox} and the graphene device dimensions. We note that improved heat sinking can be obtained by placing devices on substrates with a thinner supporting insulator⁸⁵ or higher thermal conductivity, as long as the graphene–substrate interface is not the limiting factor.^{44–46}

Recent work has also suggested that graphene devices might benefit from thermoelectric (Peltier) cooling at the metal contacts,⁹⁰ where a substantial difference in Seebeck coefficient exists. However, it is important to realize that, because of the one-dimensional nature of current flow, Peltier effects of opposite sign will occur at the two contacts, such that one cools as the other heats. Thus, additional contact engineering must be

have numerous applications, enabling efficient electrodes for fuel cells,⁹⁴ nanoporous structures with very high surface area for hydrogen storage,⁹¹ supercapacitors,⁹⁵ and tailored multi-dimensional thermal transport materials.

From the perspective of thermal transport, recent modeling studies suggest that the lateral CNT separation, called the

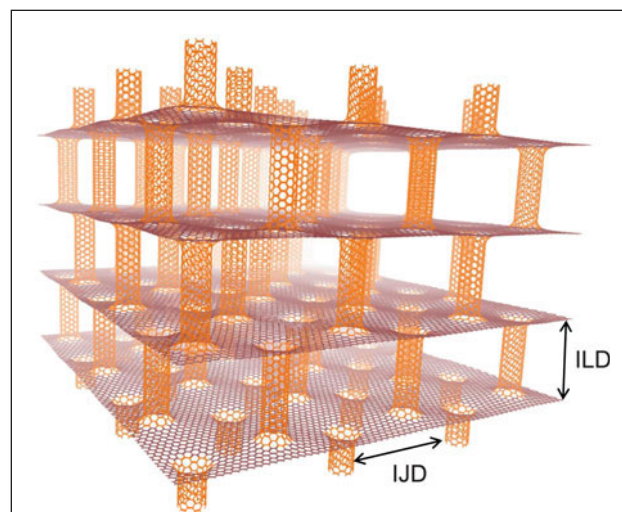


Figure 6. Schematic of a three-dimensional nanoarchitecture that combines carbon nanotube pillars and graphene sheets to achieve tunable cross-plane thermal transport. For instance, reducing the interjunction distance (IJD) and increasing the interlayer distance (ILD) could mitigate the weak interlayer thermal coupling of a graphene stack for higher cross-plane thermal conductivity. Conversely, longer IJD and shorter ILD could lower the cross-plane thermal conductivity, leading to thermal insulator or thermoelectric applications.

interjunction distance (IJD), and the interlayer distance (ILD) between graphene sheets play a critical role in determining the thermal transport properties in these 3D architectures.^{96,97} When the lateral CNT separation, IJD, is on the order of tens of nanometers, the ballistic nature of heat propagation (because of the large phonon mean free path in graphene and CNTs) causes phonon scattering to occur primarily at the CNT/graphene junction nodes. These junctions, in turn, will govern the thermal conductivity of such architectures. Furthermore, because the carbon atoms and sp^2 bonds of CNTs and graphene are the same, the phonon spectra are similar, and the junctions have very low interface thermal resistance. Hence, the thermal transport in different directions could be manipulated by tailoring the IJDs and ILDs.

For instance, the predicted interface thermal conductance at a junction^{67,68} ($\sim 10 \text{ GW m}^{-2} \text{ K}^{-1}$) is comparable to that between graphite layers ($\sim 18 \text{ GW m}^{-2} \text{ K}^{-1}$) and over two orders of magnitude higher than the graphene thermal coupling with a substrate ($\sim 50 \text{ MW m}^{-2} \text{ K}^{-1}$ at room temperature⁴⁴⁻⁴⁶). This suggests that very dense packing of long CNTs (i.e., small IJD, large ILD) could significantly increase the out-of-plane thermal conductivity of the PGN architecture, by reducing the number of interfaces and “replacing” them with CNTs.⁹⁵ On the other extreme, using short but widely spaced CNTs in the PGN structure would substantially reduce thermal conduction in the out-of-plane direction⁹⁵ (because of the small ILD, higher interface density, and low CNT areal density), thus possibly opening several routes for thermoelectric applications where extremely low thermal conductivity is desired. Over the past few years, multiple research groups have successfully synthesized CNT pillared-graphene architectures, and different property characterizations are underway.^{95,98-100}

Summary

The unusual thermal properties of graphene include very high in-plane thermal conductivity (strongly affected by interfacial interactions, atomic defects, and edges) and relatively low out-of-plane thermal conductance. The specific heat of graphene is dominated by phonons and is slightly higher than that of graphite and diamond below room temperature. The in-plane thermal conductance G of graphene can reach a significant fraction of the theoretical ballistic limit in submicrometer samples, owing to the large phonon mean free path ($\lambda \approx 100$ to 600 nm in supported and suspended samples, respectively). Nevertheless, this behavior leads to an apparent dependence of thermal conductivity κ on sample length, similar to the behavior of mobility in quasiballistic electronic devices.

In the context of integrated electronics, heat dissipation from graphene devices and interconnects is primarily limited by their environment and the relatively weak van der Waals interfaces of graphene. In the context of graphene composites and 3D architectures, simulation results have suggested that the thermal properties could be highly tunable. Such tunability raises the interesting prospects of both ultrahigh thermal conductivity for

heat-sinking applications and ultralow thermal conductivity for thermoelectric applications.

Acknowledgments

E.P. acknowledges assistance from Zuanyi Li, Andrey Serov, Pierre Martin, Ning Wang, Albert Liao, Changwook Jeong, and Mark Lundstrom, as well as funding from the AFOSR Young Investigator Program (YIP) award, the ARO Presidential Early Career (PECASE) award, and the Nanotechnology Research Initiative (NRI). V.V. and A.K.R. acknowledge Dr. Byung-Lip (Les) Lee (AFOSR Task 2302BR7P) and Dr. Joycelyn Harrison (AFOSR Task 2306CR9P) for funding from AFOSR.

References

1. H.O. Pierson, *Handbook of Carbon, Graphite, Diamond and Fullerenes: Properties, Processing and Applications* (Noyes Publications, Park Ridge, NJ, 1993).
2. M.C. Schabel, J.L. Martins, *Phys. Rev. B* **46**, 7185 (1992).
3. D.W. Bullett, *J. Phys. C: Solid State Phys.* **8**, 2707 (1975).
4. R. Saito, G. Dresselhaus, M.S. Dresselhaus, *Physical Properties of Carbon Nanotubes* (World Scientific, Singapore, 1998).
5. M. Mohr, J. Maultzsch, E. Dobardžić, S. Reich, I. Milošević, M. Damjanović, A. Bosak, M. Krisch, C. Thomsen, *Phys. Rev. B* **76**, 035439 (2007).
6. C. Oshima, T. Aizawa, R. Souda, Y. Ishizawa, Y. Sumiyoshi, *Solid State Commun.* **65**, 1601 (1988).
7. L. Wirtz, A. Rubio, *Solid State Commun.* **131**, 141 (2004).
8. N. Mingo, D.A. Broido, *Phys. Rev. Lett.* **95**, 096105 (2005).
9. D.L. Nika, E.P. Pokatilov, A.S. Askerov, A.A. Balandin, *Phys. Rev. B* **79**, 155413 (2009).
10. V.N. Popov, *Phys. Rev. B* **66**, 153408 (2002).
11. E. Muñoz, J. Lu, B.I. Yakobson, *Nano Lett.* **10**, 1652 (2010).
12. E. Pop, *Nano Res.* **3**, 147 (2010).
13. Z.-Y. Ong, E. Pop, *J. Appl. Phys.* **108**, 103502 (2010).
14. Z.-Y. Ong, E. Pop, J. Shiomi, *Phys. Rev. B* **84**, 165418 (2011).
15. K. Kang, D. Abdula, D.G. Cahill, M. Shim, *Phys. Rev. B* **81**, 165405 (2010).
16. B. Qiu, X. Ruan, *Appl. Phys. Lett.* **100**, 193101 (2012).
17. T. Tohei, A. Kuwabara, F. Oba, I. Tanaka, *Phys. Rev. B* **73**, 064304 (2006).
18. R. Nicklow, N. Wakabayashi, H.G. Smith, *Phys. Rev. B* **5**, 4951 (1972).
19. T. Nihira, T. Iwata, *Phys. Rev. B* **68**, 134305 (2003).
20. L.X. Benedict, S.G. Louie, M.L. Cohen, *Solid State Commun.* **100**, 177 (1996).
21. J. Hone, *Top. Appl. Phys.* **80**, 273 (2001).
22. L.E. Fried, W.M. Howard, *Phys. Rev. B* **61**, 8734 (2000).
23. R. Reeber, K. Wang, *J. Electron. Mater.* **25**, 63 (1996).
24. V.K. Tewary, B. Yang, *Phys. Rev. B* **79**, 125416 (2009).
25. T. Aizawa, R. Souda, Y. Ishizawa, H. Hirano, T. Yamada, K.-i. Tanaka, C. Oshima, *Surf. Sci.* **237**, 194 (1990).
26. A.M. Shikin, D. Farias, K.H. Rieder, *Europhys. Lett.* **44**, 44 (1998).
27. Z.Y. Ong, E. Pop, *Phys. Rev. B* **84**, 075471 (2011).
28. K.C. Fong, K.C. Schwab, *Phys. Rev. X* **2**, 031006 (2012).
29. C. Jeong, S. Datta, M. Lundstrom, *J. Appl. Phys.* **109**, 073718 (2011).
30. S. Chen, A.L. Moore, W. Cai, J.W. Suk, J. An, C. Mishra, C. Amos, C.W. Magnuson, J. Kang, L. Shi, R.S. Ruoff, *ACS Nano* **5**, 321 (2010).
31. A.A. Balandin, *Nat. Mater.* **10**, 569 (2011).
32. S. Chen, Q. Wu, C. Mishra, J. Kang, H. Zhang, K. Cho, W. Cai, A.A. Balandin, R.S. Ruoff, *Nat. Mater.* **11**, 203 (2012).
33. J.H. Seol, I. Jo, A.L. Moore, L. Lindsay, Z.H. Aitken, M.T. Pettes, X.S. Li, Z. Yao, R. Huang, D. Broido, N. Mingo, R.S. Ruoff, L. Shi, *Science* **328**, 213 (2010).
34. A.D. Liao, J.Z. Wu, X.R. Wang, K. Tahy, D. Jena, H.J. Dai, E. Pop, *Phys. Rev. Lett.* **106**, 256801 (2011).
35. E. Pop, D. Mann, Q. Wang, K.E. Goodson, H.J. Dai, *Nano Lett.* **6**, 96 (2006).
36. P. Kim, L. Shi, A. Majumdar, P.L. McEuen, *Phys. Rev. Lett.* **87**, 215502 (2001).
37. C.Y. Ho, R.W. Powell, P.E. Liley, *J. Phys. Chem. Ref. Data*, **1**, 279 (1972).
38. M.M. Sadeghi, M.T. Petters, L. Shi, *Solid State Commun.* **152**, 1321 (2012).
39. T.R. Anthony, W.F. Banholzer, J.F. Fleischer, L.H. Wei, P.K. Kuo, R.L. Thomas, R.W. Pryor, *Phys. Rev. B* **42**, 1104 (1990).
40. W. Jang, Z. Chen, W. Bao, C.N. Lau, C. Dames, *Nano Lett.* **10**, 3909 (2010).
41. K. Saito, J. Nakamura, A. Natori, *Phys. Rev. B* **76**, 115409 (2007).
42. M.T. Pettes, I. Jo, Z. Yao, L. Shi, *Nano Lett.* **11**, 1195 (2011).
43. R. Berman, *Phys. Rev. B* **45**, 5726 (1992).

44. Z. Chen, W. Jang, W. Bao, C.N. Lau, C. Dames, *Appl. Phys. Lett.* **95**, 161910 (2009).
45. Y.K. Koh, M.-H. Bae, D.G. Cahill, E. Pop, *Nano Lett.* **10**, 4363 (2010).
46. K.F. Mak, C.H. Lui, T.F. Heinz, *Appl. Phys. Lett.* **97**, 221904 (2010).
47. L. Lindsay, D.A. Broido, N. Mingo, *Phys. Rev. B* **82**, 115427 (2010).
48. J. Haskins, A. Kinaci, C. Sevik, H.I. Sevinçli, G. Cuniberti, T. Çağın, *ACS Nano* **5**, 3779 (2011).
49. Z. Aksamija, I. Knezevic, *Appl. Phys. Lett.* **98**, 141919 (2011).
50. W. Liu, M. Asheghi, *J. Appl. Phys.* **98**, 123523 (2005).
51. R. Chen, A.I. Hochbaum, P. Murphy, J. Moore, P. Yang, A. Majumdar, *Phys. Rev. Lett.* **101**, 105501 (2008).
52. W. Steinhögl, G. Schindler, G. Steinlesberger, M. Traving, M. Engelhardt, *J. Appl. Phys.* **97**, 023706 (2005).
53. P.G. Klemens, D.F. Pedraza, *Carbon* **32**, 735 (1994).
54. J.N. Hu, X.L. Ruan, Y.P. Chen, *Nano Lett.* **9**, 2730 (2009).
55. W.J. Evans, L. Hu, P. Keblinski, *Appl. Phys. Lett.* **96**, 203112 (2010).
56. H.J. Zhang, G. Lee, A.F. Fonseca, T.L. Borders, K. Cho, *J. Nanomater.* **2010**, 537657 (2010).
57. J.N. Hu, S. Schiffl, A. Vallabhaneni, X.L. Ruan, Y.P. Chen, *Appl. Phys. Lett.* **97**, 133107 (2010).
58. B. Mortazavi, A. Rajabpour, S. Ahzi, Y. Remond, S.M.V. Allaei, *Solid State Commun.* **152**, 261 (2012).
59. H.J. Zhang, G. Lee, K. Cho, *Phys. Rev. B* **84**, 115460 (2011).
60. W.-R. Zhong, W.-H. Huang, X.-R. Deng, B.-Q. Ai, *Appl. Phys. Lett.* **99**, 193104 (2011).
61. Y. Xu, X.B. Chen, J.S. Wang, B.L. Gu, W.H. Duan, *Phys. Rev. B* **81**, 195425 (2010).
62. Z. Huang, T.S. Fisher, J.Y. Murthy, *J. Appl. Phys.* **108**, 094319 (2010).
63. J.W. Jiang, B.S. Wang, J.S. Wang, *Appl. Phys. Lett.* **98**, 113114 (2011).
64. N. Yang, X. Ni, J.-W. Jiang, B. Li, *Appl. Phys. Lett.* **100**, 093107 (2012).
65. D. Frenkel, B. Smit, *Understanding Molecular Simulation: From Algorithms to Applications* (Academic Press, New York, ed. 2, 2002).
66. F. Hao, D.N. Fang, Z.P. Xu, *Appl. Phys. Lett.* **99**, 041901 (2011).
67. A. Bagri, S.P. Kim, R.S. Ruoff, V.B. Shenoy, *Nano Lett.* **11**, 3917 (2011).
68. A. Cao, J. Qu, *J. Appl. Phys.* **111**, 053529 (2012).
69. X. Li, K. Maute, M.L. Dunn, R. Yang, *Phys. Rev. B* **81**, 245318 (2010).
70. N. Wei, L. Xu, H.-Q. Wang, J.-C. Zheng, *Nanotechnology* **22**, 105705 (2011).
71. S.-K. Chien, Y.-T. Yang, C.O.-K. Chen, *Carbon* **50**, 421 (2012).
72. H. Sevinçli, G. Cuniberti, *Phys. Rev. B* **81**, 113401 (2010).
73. N. Yang, G. Zhang, B.W. Li, *Appl. Phys. Lett.* **95**, 033107 (2009).
74. G. Zhang, H.S. Zhang, *Nanoscale* **3**, 4604 (2011).
75. Q.-X. Pei, Y.-W. Zhang, Z.-D. Sha, V.B. Shenoy, *Appl. Phys. Lett.* **100**, 101901 (2012).
76. J. Lee, V. Varshney, A.K. Roy, J.B. Ferguson, B.L. Farmer, *Nano Lett.* **12**, 3491 (2012).
77. L. Lindsay, D.A. Broido, *Phys. Rev. B* **81**, 205441 (2010).
78. A. Javey, J. Guo, M. Paulsson, Q. Wang, D. Mann, M. Lundstrom, H. Dai, *Phys. Rev. Lett.* **92**, 106804 (2004).
79. J.-Y. Park, S. Rosenblatt, Y. Yaish, V. Sazonova, H. Üstünel, S. Braig, T.A. Arias, P.W. Brouwer, P.L. McEuen, *Nano Lett.* **4**, 517 (2004).
80. M.S. Shur, *IEEE Electron Device Lett.* **23**, 511 (2002).
81. J. Wang, M. Lundstrom, *IEEE Trans. Electron Devices* **50**, 1604 (2003).
82. R. Prasher, *Phys. Rev. B* **77**, 075424 (2008).
83. C. Jeong, R. Kim, M. Luisier, S. Datta, M. Lundstrom, *J. Appl. Phys.* **107**, 023707 (2010).
84. M.-H. Bae, S. Islam, V.E. Dorgan, E. Pop, *ACS Nano* **5**, 7936 (2011).
85. A. Behnam, A.S. Lyons, M.-H. Bae, E.K. Chow, S. Islam, C.M. Neumann, E. Pop, *Nano Lett.* **12**, 4424 (2012).
86. A. Barreiro, M. Lazzeri, J. Moser, F. Mauri, A. Bachtold, *Phys. Rev. Lett.* **103**, 076601 (2009).
87. V.E. Dorgan, M.H. Bae, E. Pop, *Appl. Phys. Lett.* **97**, 082112 (2010).
88. V. Perebeinos, P. Avouris, *Phys. Rev. B* **81**, 195442 (2010).
89. K. Kang, D. Abdula, D.G. Cahill, M. Shim, *Phys. Rev. B* **81**, 165405 (2010).
90. K.L. Grosse, M.H. Bae, F.F. Lian, E. Pop, W.P. King, *Nat. Nanotechnol.* **6**, 287 (2011).
91. G.K. Dimitrakakis, E. Tylisanakis, G.E. Froudakis, *Nano Lett.* **8**, 3166 (2008).
92. E. Tylisanakis, G.K. Dimitrakakis, S. Melchor, J.A. Dobado, G.E. Froudakis, *Chem. Commun.* **47**, 2303 (2011).
93. Z.P. Chen, W.C. Ren, L.B. Gao, B.L. Liu, S.F. Pei, H.M. Cheng, *Nat. Mater.* **10**, 424 (2011).
94. W. Zhang, P. Sherrell, A.I. Minett, J.M. Razal, J. Chen, *Energy Environ. Sci.* **3**, 1286 (2010).
95. F. Du, D.S. Yu, L.M. Dai, S. Ganguli, V. Varshney, A.K. Roy, *Chem. Mater.* **23**, 4810 (2011).
96. V. Varshney, S.S. Patnaik, A.K. Roy, G. Froudakis, B.L. Farmer, *ACS Nano* **4**, 1153 (2010).
97. V. Varshney, A.K. Roy, G. Froudakis, B.L. Farmer, *Nanoscale* **3**, 3679 (2011).
98. R.K. Paul, M. Ghazinejad, M. Penchev, J.A. Lin, M. Ozkan, C.S. Ozkan, *Small* **6**, 2309 (2010).
99. L.L. Zhang, Z.G. Xiong, X.S. Zhao, *ACS Nano* **4**, 7030 (2010).
100. K.H. Yu, G.H. Lu, Z. Bo, S. Mao, J.H. Chen, *J. Phys. Chem. Lett.* **2**, 1556 (2011). □



SAVE THE DATE

10th International Conference on Nitride Semiconductors | August 25-30, 2013
Gaylord National Hotel and Convention Center—Washington, D.C.

IMPORTANT DATES:

ABSTRACT SUBMISSION OPENS Early February 2013

ABSTRACT SUBMISSION ENDS Mid-April 2013

PREREGISTRATION OPENS Mid-April 2013

PREREGISTRATION ENDS Early August 2013

Join us for the 10th International Conference on Nitride Semiconductors 2013 (ICNS-10). Held just outside historic Washington, D.C., the Conference will present high-impact scientific and technological advances in materials and devices based on group-III nitride semiconductors. The Conference will feature plenary sessions, parallel topical sessions, poster sessions and an industrial exhibition. Mark your calendar today and plan to attend ICNS-10!

Scientific Program

The six-day Conference will concentrate on the following topical categories:

- Bulk Crystal Growth
- Epitaxial Growth
- Optical and Electronic Properties
- Processing and Fabrication
- Defect Characterization and Engineering
- Structural Analysis
- Theory and Simulation
- Nanostructures
- Light Emitting Devices
- Electron Transport Devices
- Photovoltaics and Energy Harvesting
- New Materials and New Device Concepts

Conference Venue

ICNS-10 will be held at the beautiful National Harbor, located on the banks of the Potomac River. This unique, ever expanding complex, offers something interesting and different for everyone in the family. Featuring numerous shopping, dining and entertainment venues, the waterfront community brings the finest options from land or water. Just minutes from the harbor, find one of the world's cultural, government and historic epicenters—Washington, D.C. The architecture, monuments, museums and cultural diversity add up to one ideal Conference and vacation destination.

For the most up-to-date information on ICNS-10, visit www.ICNS10.org or the Conference website, www.mrs.org/ICNS-10.

